How Deep Hole Traps Affect the Charge Dynamics and Collection in Bare and Bilayers of Methylammonium Lead Bromide

Zhao, Jiashang; Caselli, Valentina M.; Bus, Marcel; Boshuizen, Bart; Savenije, Tom J.

Important note
To cite this publication, please use the final published version (if applicable).
Please check the document version above.

How Deep Hole Traps Affect the Charge Dynamics and Collection in Bare and Bilayers of Methylammonium Lead Bromide

Jiashang Zhao, Valentina M. Caselli, Marcel Bus, Bart Boshuizen, and Tom J. Savenije*

Cite This: *ACS Appl. Mater. Interfaces* 2021, 13, 16309−16316

Read Online

ACCESS | Metrics & More | Article Recommendations | Supporting Information

ABSTRACT: Wide-band-gap perovskites such as methylammonium lead bromide (MAPB) are promising materials for tandem solar cells because of their potentially high open-circuit voltage, which is yet still far below the maximum limit. The relatively short charge-carrier lifetimes deduced from time-resolved photoluminescence (TRPL) measurements seem in strong contrast with the long lifetimes observed with time-resolved photo-conductance measurements. This is explained by a large amount of hole defect states, $N_T > 10^{16}$ cm^{-3}, in spin-coated layers of MAPB residing at or near the grain boundaries. The introduction of hypophosphorous acid (HPA) increases the average grain size by a factor of 3 and reduces the total concentration of the trap states by a factor of 10. The introduction of HPA also increases the fraction of initially generated holes that undergo charge transfer to the selective contact, Spiro-OMeTAD (SO), by an order of magnitude. In contrast to methylammonium lead iodide (MAPI)/SO bilayers, a reduction of the carrier lifetime is observed in MAPB/SO bilayers, which is attributed to the fact that injected holes undergo interfacial recombination via these trap states. Our findings provide valuable insight into the optoelectronic properties of bromide-containing lead halide perovskites essential for designing efficient tandem solar cells.

KEYWORDS: *metal halide perovskites, time-resolved microwave conductivity, deep hole traps, charge-carrier dynamics, charge selective contact*
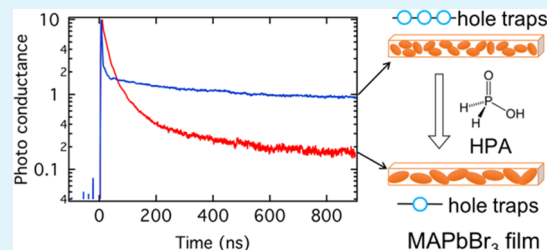
INTRODUCTION

Metal halide perovskites (MHPs) have attracted an increasing amount of attention over the past decade due to the steep increase in performance of MHP-based solar cells from an initial 3.8% in 2009 to over 25%.[1−6] The high performance is attributed to a number of interesting properties such as high optical absorption coefficients, long charge-carrier diffusion lengths, and recombination lifetimes as well as low trap state densities.[4,7,8] Their low cost and ease of processing make them also attractive for other applications including light-emitting diodes, lasers, and X-ray detectors.[9−11] Recently, tandem solar cells based on a Si bottom cell and a MHP top cell are intensively investigated since efficiencies above the Shockley−Queisser limit can be attained.[12−15] The wide band gap of 2.38 eV of methylammonium lead bromide (MAPB) perovskite makes it a promising candidate as a top cell for a tandem solar cell.[16,17] Moreover, MAPB features promising properties, such as high photoluminescence (PL) yield,[18] relatively small exciton binding energies,[19] and balanced mobility between electrons and holes.[17] In principle, the wider band gap of MAPB should potentially allow for higher open-circuit voltages (V_{oc}) essential to reach higher power conversion efficiencies (PCEs) of tandem solar cells. However, in practice, the energy gap between the E_{bg}/e and V_{oc} for mixed halide perovskites increases with the increasing ratios of Br/I.[20] For MAPB-based solar cells, the maximum reported V_{oc}'s amounts to 1.61 V,[21]

which in view of the E_{bg} of 2.38 eV yields a deficit of 0.77 V. In comparison, for MAPI, E_{bg} amounts to 1.59 eV and the highest reported voltage amounts to 1.26 V, yielding a gap of only 0.33 V.[22] Hence, to reach higher V_{oc}'s for the Br-containing top cell, a detailed understanding and eventual reduction of this deficit is important.

One of the most critical factors determining the efficiency of MHP-based solar cells is the presence of recombination centers. For perovskites, a large variety of defect states including point defects in the bulk, e.g., interstitials or vacancies and surface defects, such as undercoordinated halides ions or lead ions, is possible. Some of these defects form states within the forbidden band gap and lead to the trapping of excess charge carriers.[23,24] Hence, to ultimately improve solar cell efficiencies, it is particularly important to understand the origin and type of these trap states. From density functional theory calculations,[25] it has been reported that halide interstitials and lead vacancies are the most stable defects in both MAPI and MAPB. For both these materials, it
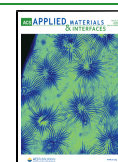
is argued that halide interstitials result in slight p-type behavior. In another work, Musiienko et al. found by first-principle calculations that cation vacancies and Br interstitials are the main acceptors in MAPB.[26] However, there are no detailed experimental studies focusing on the density and the type of trap states as well as the relationship between structure and trap states in MAPB perovskites.

In this work, time-resolved microwave conductivity (TRMC) was used to study trap states in bare MAPB and in bilayers of MAPB with a charge selective transport layer. We start off by comparing the time-resolved PL and time-resolved photoconductance measurements on MAPB with those on MAPI. These data suggest that one type of carrier in MAPB is trapped on short timescales resulting in photoconductance decays extending into the multi-microsecond time regime. Furthermore, we investigate how these trap states are affected by the domain size, which we manipulate by the addition of a small percent of hypophosphorous acid (HPA) to the precursor solution. Previous research on the addition of HPA has improved the electronic properties of MAPI layers remarkably. In that work, it is argued that HPA, a strong reducing agent, avoids the oxidation of I⁻ and in addition retards the crystallization process yielding larger crystals.[27−29] Analysis of the TRMC traces of MAPB-HPA shows a reduction of the number of trap states by an order of magnitude, which is related to the increased grain size as exposed by atomic force microscopy (AFM). Additional PL and TRMC measurements on MAPB/SO and MAPB/C_{60} bilayer systems allowed us to determine the type of deep traps. Finally, we modeled the charge-carrier dynamics in the single and bilayers to extract hole transfer rates and charge-carrier collection efficiencies. Our findings provide valuable insight into how passivation of deep trap states in MAPB affects the charge-carrier dynamics, essential for optimizing perovskite-based optoelectronic devices and designing tandem solar cells.

RESULTS AND DISCUSSION

MAPB thin films (~300 nm) were deposited on precleaned quartz substrates by spin-coating a N,N-dimethylformamide (DMF) solution containing the precursors methylammonium bromide (MABr) and lead acetate trihydrate in a 3:1 molar ratio. MAPI thin films (~250 nm) were prepared using the same procedure, with methylammonium iodide replacing MABr. The (100), (200) and (110), (220) main characteristic peaks in the X-ray diffraction (XRD) patterns (SI, Figure S1) confirm the cubic and tetragonal crystal structure of MAPB and MAPI films, respectively.[30] Absorption and fluorescence spectra of MAPI are provided in the SI, Figure S2 and correspond to previously reported spectra.[31]

Figure 1a,b shows photoconductance traces (ΔG) normalized by the number of absorbed photons as a function of time on photoexcitation of MAPI (λ = 650 nm) and MAPB (λ = 500 nm) in a log-linear representation. The initial increase of the signal originates from the generation of free charge carriers, while the decay is attributed to recombination or to the immobilization of excess carriers by trapping. The traces recorded for MAPI are similar to those reported previously by some of us.[8,32,33] The signal heights for MAPI are substantially higher than that for MAPB, which can be attributed to the lower charge-carrier mobilities for the latter.[34] On increasing the laser intensity, the decay kinetics become faster, which can be explained by the fact that with higher initial charge densities the second-order band-to-band recombination leads to faster
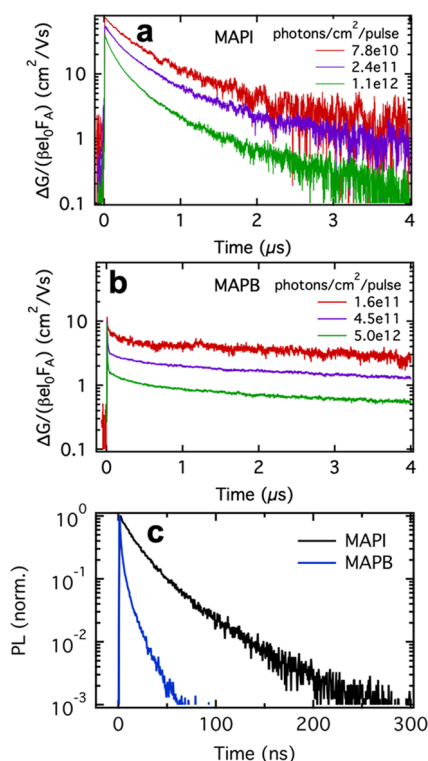

Figure 1. Photoconductance as a function of time for (a) MAPI and (b) MAPB recorded at intensities ranging from 10^{10} to 10^{12} photons cm^{-2} per pulse, corresponding to initial charge-carrier densities of 10^{15}–10^{17} cm^{-3}. (c) PL lifetimes of MAPI and MAPB thin films recorded using pulsed excitation at 405 nm.

decay. Most intriguingly, the decay kinetics for the MAPB are substantially different compared to MAPI. Although at higher intensities the decay kinetics are initially faster, all traces are characterized by almost parallel tails at longer times, even extending into the microsecond timescales. Moreover, the same trend was also observed in MAPB films prepared from PbBr$_2$ (see the SI, Figure S3), which indicates that these long tails are independent of the lead precursor source. Furthermore, similar long-lived photoconductance and transient absorption traces have been previously reported for bromide-rich MHPs.[25,35]

The time-resolved photoluminescence (TRPL) traces for both materials displayed in Figure 1c show the opposite behavior: the lifetime of MAPB is substantially shorter than that of MAPI. Since the PL originates from the radiative decay of electrons and holes,[36] this observation implies that in MAPB one type of charge carrier is depleted within few tens of nanoseconds. At the same time, we can deduce that the other type of charge carrier is mobile for prolonged timescales, as it is apparent from the TRMC traces. These results suggest that for MAPB, one type of carrier, is trapped on short timescales resulting in a rather different photophysical behavior in comparison to MAPI.

To further investigate the nature and origin of the trap states in MAPB, HPA was added to the precursor solution to manipulate the morphology of MAPB yielding thin films, denoted as MAPB-HPA.[27] HPA has been used as an additive in the MAPI and MAPI$_{3−x}$Cl$_x$ to improve the optoelectronic properties.[27−29,37] The XRD pattern of MAPB-HPA is very comparable to the pattern of the perovskite layer without HPA, denoted as MAPB-reference (MAPB-ref) (see the SI, Figure
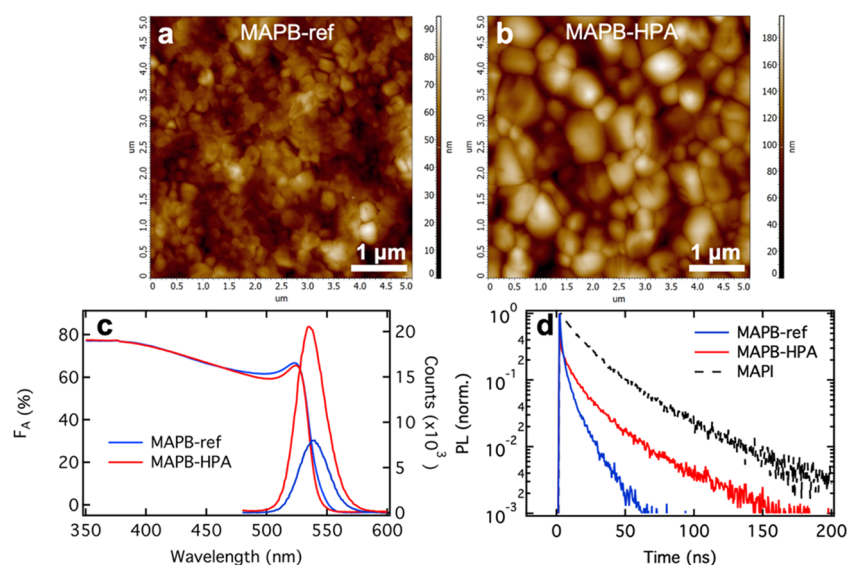
Figure 2. Atomic force microscopy (AFM) images for MAPB-ref- (a) and MAPB-HPA-processed (b) films spin-coated on quartz substrates. (c) Fraction of light absorbed (F_A) by MAPB-ref and MAPB-HPA films (left axis) and corresponding PL spectra (right axis). (d) PL lifetimes of MAPB-ref and MAPB-HPA thin films photoexcited at 405 nm (1 MHz, 1.2×10^{12} photons cm^{-2}) recorded at the maximum emission wavelengths.
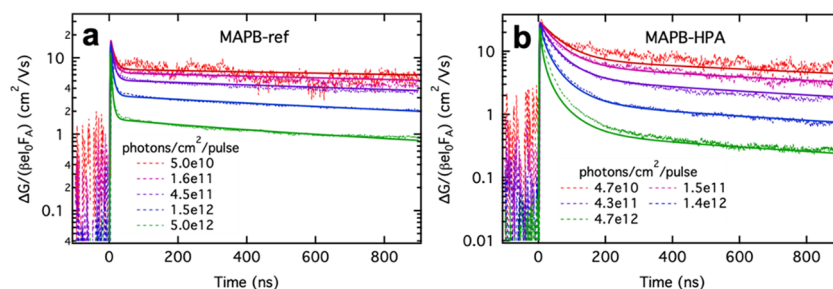

Figure 3. Photoconductance as a function of time for MAPB-ref (a) and processed with HPA (b) thin films for intensities ranging from 10^{10} to 10^{12} photons cm^{-2} per pulse ($\lambda = 500$ nm), corresponding to initial charge-carrier densities of $10^{15}-10^{17}$ cm^{-3}. The full lines are fits to the data points as described in the text.

S1). From X-ray photoemission spectroscopy (see the SI, Figure S4), we observe only a small amount of P (2.5%) in the MAPB-HPA layer.

Figure 2a,b shows the atomic force microscopy (AFM) images of both MAPB films, respectively. It is apparent that the average perovskite domain size is significantly enlarged on adding HPA: from ca. 200 to 700 nm. The substantial increase of the domain size in the HPA sample is due to the lower crystallization rate during the nucleation of perovskite, as previously reported.[28] Therefore, the total surface area related to the domain boundaries in MAPB-HPA is considerably smaller than in the MAPB-ref.

Then, we investigated the optical properties of these two MAPB perovskites layers. Figure 2c displays the fraction of absorbed light (F_A) and the PL emission of both thin films. For both samples, we find the contribution of the characteristic excitonic absorption at 524 nm to the absorption spectra. For MAPB-ref, a small red shift of approximately 5 nm of the absorption onset and of the maximum PL are observed. More importantly, the PL intensity of MAPB-HPA is about 4 times higher than that of MAPB-ref. Furthermore, TRPL measurements show that the PL lifetime of MAPB-HPA is increased by a factor of 2 in comparison to MAPB-ref. The improved optical properties of MAPB-HPA are expected to result from suppressed nonradiative recombination pathways due to the

reduction of the number of trap states.[38] Assuming that the trap states are largely located at the grain surface, this decrease might be reasonably related to the reduced total surface area of MAPB-HPA.

To gain more insight into the trapping process by intraband-gap states, we measured the photoconductance traces in MAPB-ref and MAPB-HPA thin films (see Figure 3). A number of observations can be made on addition of HPA: first, the maximum signal height is higher. This value represents the product of the free charge-carrier generation yield, φ, and the sum of the electron and hole mobility, $\sum \mu$. Based on the thermal energy at 300 K and the exciton binding energy of MAPB, which is in the range of 14−60 meV,[19,39] we expect that the predominant part of the excitons is dissociated into free charges as detailed in the SI (Figure S5). Therefore, we can assume that φ is close to unity at room temperature for both samples. Apart from this increased signal height, we observe a substantial reduction in the initial decay kinetics on addition of HPA. To extract the mobilities and rate constants for various processes, we modeled photoconductance traces using a kinetic model (see Scheme 1) previously successfully used to describe the photophysical processes in MAPI.[8,35] For MAPB, the fits are calculated by taking into account the processes indicated by the black arrows and assuming a slightly n-doped material as will be discussed later on (see the SI for a

Scheme 1. Kinetic Model of Charge-Carrier Processes Initiated by Photoexcitation of MAPB[a]
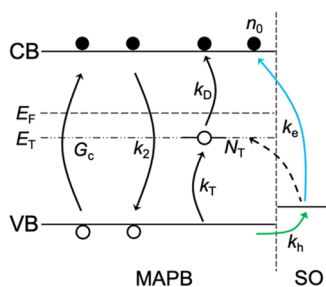
[a]G_c represents the photogeneration of charge carriers; k_2 depicts the second-order recombination rate. Hole trap-mediated recombination is described by a trapping rate k_T and depopulation rate k_D. The Fermi level, E_F, is located above the trap level, E_T, implying that the material is n-type doped. In the presence of a SO hole transport layer, charges can be injected into SO with k_h (green arrow) and further recombine with electrons via k_e (blue arrow).

used set of differential eqs S2−S4). The fits are added in Figure 3 as solid lines and are in good agreement with the experimental traces. All kinetic parameters are collected in Table 1.

The $\sum \mu$ values are 19 and 30 cm^2 V^{-1} s^{-1} for MAPB-ref and MAPB-HPA, respectively. We attribute this increase to the expanded domain sizes of MAPB-HPA since the measured mobility at 8.5 GHz can be reduced by the domain boundaries. The resulting restriction in the charge-carrier motion reduces the measured effective AC mobility.[40] Also, k_2 representing the second-order recombination process is reduced from 5.5×10^{-9} to 2.1×10^{-9} cm^3 s^{-1}. In addition to radiative band-to-band recombination, nonradiative trap-mediated decay can also give rise to the second-order decay process as we and others have experimentally observed.[8,36] Obviously, the reduced surface area of MAPB-HPA has resulted in a lowering of the nonemissive part of k_2. This agrees with the enhancement in PL for the MAPB-HPA film. More importantly, the concentration of deep trap states, N_T, for MAPB-HPA is 1 order of magnitude lower as compared to the ref sample. The origin of the reduction of N_T could be attributed to the reduced total surface area of the MAPB-HPA layer. Moreover, the substantially higher N_T values in MAPB in comparison to those reported for MAPI[32] explain the differences observed with (TR)PL and TRMC, as shown in Figure 1.

Knowing the rate constants for the various processes allows us to model the TRPL signal, which is given by[8]

$$\text{TRPL} = k_2[n + n_0][p] \qquad (1)$$

Since the laser pulse used for time-correlated single-photon counting (TCSPC) measurements is different from the TRMC experiments, we have to adapt the G_C term in the set of coupled differential equations (see the SI, eqs S2−S4). Solving the equations again numerically yields the time-dependent concentrations of n and p. Via this approach, the TRPL signals for both MAPB films are calculated and shown in the SI, Figure S6. Although there is no exact match with Figure 2d, the similarity with experimental TRPL traces is clearly present.

To obtain more information about the type of traps and how trap states affect the charge collection, we deposited Spiro-OMeTAD (SO) (∼250 nm) as a hole transport layer or C$_{60}$ as an electron transport layer (∼30 nm) on top of the same perovskite layers studied above. The absorption spectra of SO and C$_{60}$ as well as their corresponding bilayers are shown in the SI, Figure S7. For all bilayers, we observe a clear reduction in PL intensity on the introduction of SO as well as of C$_{60}$ in comparison with the bare MAPB layer, indicating charge transfer to the transport layer. For the bilayers based on MAPB-HPA, the PL quenching was substantially stronger than for the MAPB-ref based bilayers (SI, Figure S8). In Figure 4, the normalized photoconductance traces of the bare ref and HPA perovskites together with their bilayer systems are shown. The samples were excited through the transport layer using an excitation wavelength of 500 nm. The non-normalized traces are provided in the SI, Figure S10.

For MAPB-ref/SO, a relatively small deviation from the single layer is visible, while for MAPB-HPA/SO, the tail of the TRMC signal is decaying much faster than the base layer (see also the SI, Figure S9a,b for a log-linear representation). Note that the mobility of charges in SO (and also in C$_{60}$) is more than an order of magnitude smaller than in MHPs and that only mobile carriers contribute to the photoconductance.[41,42] The fact that the introduction of the SO layer on the MAPB-ref layer does not appreciably change the TRMC trace demonstrates that the holes do not contribute substantially to the TRMC signal in neither the bare layer nor the bilayer. Hence, in both samples, the excess electrons are responsible for the TRMC signal. From here, we can conclude that the majority of the excess holes in the bare MAPB-ref layer are rapidly trapped. Holes captured in trap states are not mobile and thus do not contribute to the conductance. This result is understandable in view of the initial charge-carrier density of 3×10^{15} cm^{-3} and the much larger value of N_T for the MAPB-ref. For the MAPB-HPA/SO bilayer, the situation is somewhat different since N_T is close to the initial charge-carrier density and hence partial hole transfer can be expected. As mentioned above, those injected holes in SO hardly contribute to photoconductance due to their low mobility. From the faster decay kinetics for both bilayers in comparison to the bare

Table 1. Kinetic Fitting Parameters Extracted from TRMC Traces for Bare MAPB and MAPB/SO Bilayers

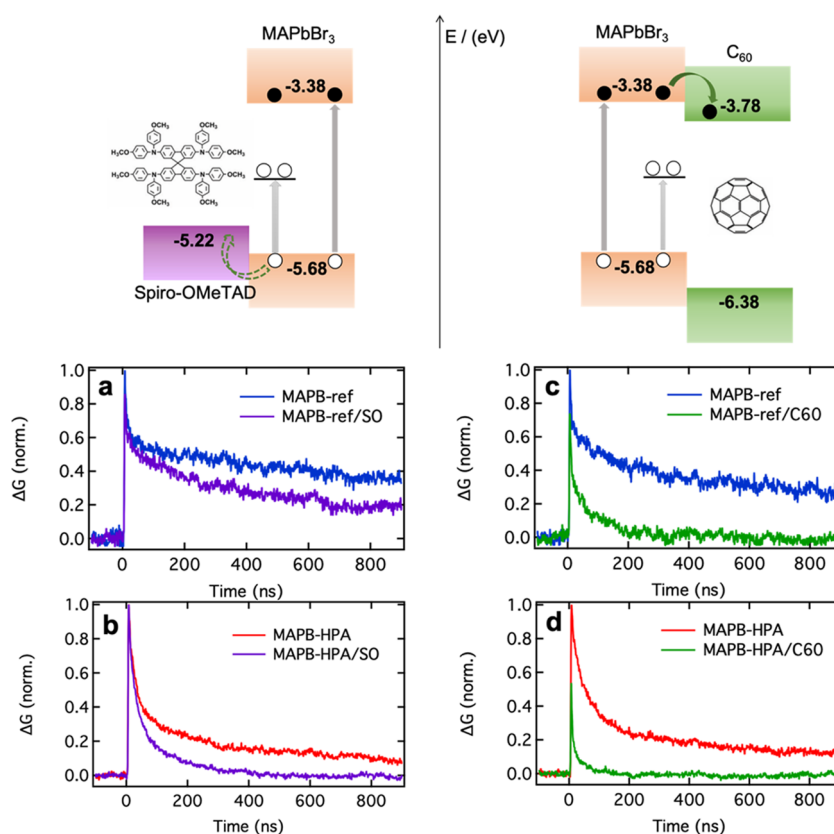|	MAPB-ref	MAPB-ref/SO	MAPB-HPA	MAPB-HPA/SO
k_2 [$\times 10^{-9}$ cm^3 s^{-1}]	5.5	6.5	2.1	2.8
k_T [$\times 10^{-9}$ cm^3 s^{-1}]	2	2	2.5	2.5
k_D [$\times 10^{-10}$ cm^3 s^{-1}]	0.45	3.2	1.5	50
N_T [$\times 10^{15}$ cm^{-3}]	35	35	3.5	3.5
n_0 [$\times 10^{15}$ cm^{-3}]	3.5	3.5	3.5	3.5
k_h [$\times 10^6$ s^{-1}]		5		10
k_e [$\times 10^6$ s^{-1}]		<0.1		7
$\sum \mu$ [cm^2 V^{-1} s^{-1}]	19	19	30	30

Figure 4. Energy diagrams and charge-carrier processes occurring upon photoexcitation of MAPB/SO (top, left) and MAPB/C_{60} (top, right). TRMC traces for neat MAPB and MAPB/SO bilayers (a, b) and MAPB/C_{60} bilayers (c, d) for both ref (a, c) and HPA processed (b, d) samples recorded at initial charge-carrier densities of 3×10^{15} cm^{-3} ($\lambda = 500$ nm). Maximum signal sizes of single layers are normalized to 1, while bilayers are normalized with the same factor.

MAPB layers, we conclude that the recombination of holes with the mobile conduction band electrons is enhanced by the introduction of SO, which we will discuss in more detail below.

For both MAPB/C_{60} bilayers, we observe a drop in the initial signal size and a severe reduction in a lifetime as compared to the single perovskite layer (a log-linear representation is shown in the SI, Figure S9c,d). The reduction of the initial photoconductance could be partially due to the fact that C_{60} has a nonzero absorption at 500 nm. More importantly, the long-lived tails clearly visible in the bare MAPB layer disappear in both MAPB/C_{60} bilayers. Realizing that the dominant part of the holes is trapped in the MAPB layer, and the fact that the TRMC signal goes quickly back to zero, proves that electron transfer from both MAPB layers into C_{60} is efficient which is in accordance with the PL quenching.

The above explanation for the TRMC measurements on the double layers brings us to the conclusion that the dominant type of traps in MAPB layers are hole traps. Then, we examine the decay kinetics in both MAPB/SO bilayers. For both bilayers, we observe a reduction in charge-carrier lifetime with those in bare MAPB layers. In contrast, we reported previously for MAPI/SO bilayers an enhancement in charge-carrier lifetimes, which was attributed to the fact that after charge transfer the charges are physically separated.[31,32] To obtain more insight into the recombination processes, we fitted the bilayers using the kinetic model of Scheme 1 completed by an additional charge transfer process to the transport layer with rate constant k_h and recombination of a hole in SO with a conduction band electron with rate k_e as indicated in green and

blue, respectively. The TRMC traces and corresponding fits are provided in the SI, Figure S11, for a range of intensities. The used kinetic parameters are added to Table 1. For both MAPB/SO bilayers, we observe values of $5-10 \times 10^6$ s^{-1} for k_h, which confirms that hole transfer to the transport layer occurs. Although most found parameters are very comparable to the corresponding bare MAPB, we observe an increase of more than an order of magnitude for k_D. Obviously, the introduction of SO enhances the emptying of occupied trap states. To explain this observation, we argue that (i) the location of the trap states is near or at the surface of the grains. This explains that for MAPB-HPA the effect is more severe than for the MAPB-ref layer since for the latter most of the grain boundaries are not in direct contact with SO. (ii) The energetic position of the trap states is located close to or above the highest occupied molecular orbital (HOMO) level of SO. In this way, the surface states offer an additional decay path for holes that have been injected into SO, as indicated by the dashed arrow in Scheme 1. The increased decay rate from the trap states can be attributed to the fact that the injected holes in SO induce an internal electric field pulling electron density toward the interface. The increased electron concentration enhances the recombination of trapped holes with conduction band electrons. Both effects lead basically to an increase of the trap-mediated recombination, which might be one of the key reasons for the higher voltage deficit in the MAPB-based cells in comparison to the MAPI cells. However, we cannot exclude that also the fast interfacial recombination observed at the interface between MAPB/C60 might be another reason for the

voltage deficit. The lower concentration or absence of surface states for MAPI explains why, in contrast to MAPB/SO bilayers, an elongation of the charge-carrier lifetimes on hole transfer to SO is observed (see the SI, Figure S12).[31,32]

Knowing all of the rate constants describing the bare and bilayer system allows us to determine the fraction of the initially generated excess carriers by the laser pulse, which has undergone charge transfer into SO. For both bilayers, this fraction is displayed in Figure 5 versus the laser intensity. In
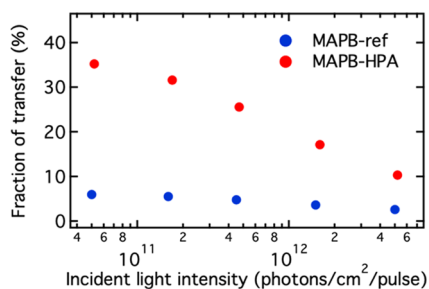

Figure 5. Fraction of initial photoinduced charge carriers that undergo charge transfer to the SO transport layer.

particular, at low intensities where the second-order recombination is less prominent, we can conclude that the charge collection for the MAPB-ref is almost a factor of 10 less efficient. This is in line with the much weaker PL quenching efficiency in the MAPB-ref/SO bilayer than in MAPB-HPA/SO. Although under steady-state illumination conditions the results may be somewhat different, we conclude that for MAPB-ref/SO hole collection is hampered, reducing the efficiency of a MAPB-ref based solar cell.

Combining all found information regarding the trap states in MAPB brings us to the following key features: spin-coated MAPB is characterized by a large amount of defect hole states, $N_T > 10^{16}$ cm^{-3}, residing at or near the surface of the perovskite grains. The introduction of HPA in the spin-coating solution considerably increases the grain sizes and at the same time reduces the total concentration of the trap states by an order of magnitude. As mentioned in the Introduction section, undercoordinated atoms at the surface might give rise to such surface traps. The larger crystals of the MAPB-HPA layer resulting in the reduced surface area of the MAPB-HPA layer is likely the major origin of the reduced concentration of the defect states.

CONCLUSIONS

In this work, the optoelectronic properties of MAPB, which are markedly different from those of MAPI, are described, in particular how trap states affect the charge-carrier dynamics and charge collection. By addition of HPA to the precursor solution, the average crystal domain size is found to increase by more than a factor of 3, as revealed by AFM. Analysis of the photoconductance traces recorded by electrodeless time-resolved microwave measurements reveals that positive charges are trapped on short timescales. Most importantly, the concentration of deep trap states, N_T, for MAPB-HPA is reduced from 35×10^{15} to 3.5×10^{15} cm^{-3}. Furthermore, k_2 comprising both radiative and nonradiative second-order recombination is reduced by a factor of 2. Both observations can be attributed to the reduced surface area of MAPB-HPA. From additional PL and TRMC measurements on MAPB-ref/

SO and MAPB-HPA/C_{60} double layers, we conclude that charge transfer into C_{60} and SO occurs. However, for MAPB-ref/SO, the hole collection is hampered by the presence of excessive amounts of hole traps. In contrast to MAPI/SO, we observe a reduction of the charge-carrier lifetime in bilayers, which we attribute to the fact that interfacial recombination from the injected holes via the trap states is possible. More insight into the manipulation of the concentration of intra-band-gap states and in their effect on the charge-carrier dynamics will contribute to a more complete understanding of the optoelectronic properties of MAPB. This is essential for optimizing perovskite-based optoelectronic devices in particular for bromide-containing perovskite top cells for application in tandem solar cells.

EXPERIMENTAL METHODS

Preparation of MHP Films. Quartz substrates were rinsed with acetone and ethanol in an ultrasonic bath for 10 min each. Subsequently, oxygen plasma treatment was performed prior to layer deposition. To prepare MAPB/MAPI precursor solution, methylamine bromide (336 mg, 3.0 mmol)/methylamine iodide (480 mg, 3.0 mmol) and lead acetate trihydrate (PbAc$_2$·3H$_2$O) (379 mg, 1.0 mmol) were dissolved in anhydrous N,N-dimethylformamide (DMF) (1.77 mL). For the preparation of the MAPB-HPA layers, 4 μL of an HPA stock solution was added to the precursor solution yielding a 7.5% molar ratio of HPA to PbAc$_2$. The perovskite solutions were spin-coated on the substrates at 2000 rpm for 45 s and then annealed at 100 °C for 5 min after drying for 10 min at room temperature. For the Spiro-OMeTAD layer, a 75 mg mL^{-1} chlorobenzene solution was prepared, which was spin-coated at 1500 rpm for 45 s. The C_{60} layer (30 nm) was thermally evaporated.

Photoconductance Measurements. The time-resolved microwave conductivity (TRMC) technique was determined to investigate the photoconductance as a function of time using an excitation wavelength of 500 nm for MAPB and 650 nm for MAPI. With this technique, the reduction in microwave power ($\Delta P(t)/P$) induced by a laser pulse (repetition rate: 10 Hz) was related to the change in conductance ($\Delta G(t)$) by the sensitivity factor K

$$\frac{\Delta P(t)}{P} = -K\Delta G(t) \tag{2}$$

The TRMC signal is expressed in the product of mobility ($\mu_e + \mu_h$) and charge-carrier yield φ, which was calculated from the maximum change in photoconductance ΔG_{max}

$$\varphi(\mu_e + \mu_h) = \frac{\Delta G_{max}}{F_A I_0 e \beta} \tag{3}$$

where F_A is the fraction of light absorbed by the sample at the excitation wavelength, I_0 is the laser intensity in the number of photons per unit area per pulse, e is the elementary charge, and β is the ratio of the inner dimensions of the microwave cell. The samples were placed in a sealed microwave cell inside the glovebox to ensure that they are not exposed to ambient conditions during the measurement.

Optical Characterization. Absorption spectra were recorded with a PerkinElmer Lambda 1050 spectrophotometer equipped with an integrated sphere. The samples were placed inside the sphere to measure the total fraction of reflected and transmitted light (F_{R+T}). Then, the fraction of absorbed light (F_A) was calculated by

$$F_A = 1 - F_{R+T} \tag{4}$$

Photoluminescence spectra and lifetimes in the main text were carried out using an Edinburgh LifeSpec spectrometer equipped with a single-photon counter. The films were excited at 405 nm using a picosecond pulsed diode laser ($I_0 = 1.2 \times 10^{12}$ photos/cm^2) at 1 MHz. On recording the transients at a repetition rate limited to 100 kHz, no significant changes were observed. Photoluminescence spectra in the

Structural Characterization. X-Ray diffraction patterns were conducted on a Brucker D8 diffractometer in a Bragg−Brentano configuration using Co-Kα (λ = 1.79 Å) radiation.

The atomic force microscopy measurements were performed on a NTMDT Ntegra Aura AFM system in semicontact mode. The cantilevers used were Nanosensors PPP-NCHR with a resonance frequency of 350 kHz. The only postprocessing performed was a linear line by line flattening.

X-ray photoemission spectroscopy (XPS) measurements were conducted using a Thermo Fisher K-Alpha surface analysis machine.

■ ASSOCIATED CONTENT

ⓈⒾ Supporting Information

The Supporting Information is available free of charge at https://pubs.acs.org/doi/10.1021/acsami.1c00714.

> Structural and optical analyses; a detailed description of the Saha equation; detailed MAPB/C60 and MAPB/SO bilayer analyses; and additional TRPL and TRMC fits (PDF)

■ AUTHOR INFORMATION

Corresponding Author

Tom J. Savenije − *Department of Chemical Engineering, Delft University of Technology, 2629 HZ Delft, The Netherlands;* ⓞ orcid.org/0000-0003-1435-9885; Email: T.J.Savenije@tudelft.nl

Authors

Jiashang Zhao − *Department of Chemical Engineering, Delft University of Technology, 2629 HZ Delft, The Netherlands*

Valentina M. Caselli − *Department of Chemical Engineering, Delft University of Technology, 2629 HZ Delft, The Netherlands;* ⓞ orcid.org/0000-0002-3730-5241

Marcel Bus − *Department of Chemical Engineering, Delft University of Technology, 2629 HZ Delft, The Netherlands*

Bart Boshuizen − *Department of Chemical Engineering, Delft University of Technology, 2629 HZ Delft, The Netherlands*

Complete contact information is available at:
https://pubs.acs.org/10.1021/acsami.1c00714

Notes

The authors declare no competing financial interest.

■ ACKNOWLEDGMENTS

■ REFERENCES

(1) Heo, J. H.; Im, S. H.; Noh, J. H.; Mandal, T. N.; Lim, C.-S.; Chang, J. A.; Lee, Y. H.; Kim, H.-J.; Sarkar, A.; Nazeeruddin, M. K.; Grätzel, M.; Seok, S. I. Efficient Inorganic−Organic Hybrid Heterojunction Solar Cells Containing Perovskite Compound and Polymeric Hole Conductors. *Nat. Photonics* **2013**, *7*, 486−491.

(2) Im, J. H.; Lee, C. R.; Lee, J. W.; Park, S. W.; Park, N. G. 6.5% Efficient Perovskite Quantum-Dot-Sensitized Solar Cell. *Nanoscale* **2011**, *3*, 4088−4093.

(3) Kim, H.-S.; Lee, C. R.; Im, J. H.; Lee, K. B.; Moehl, T.; Marchioro, A.; Moon, S. J.; Humphry-Baker, R.; Yum, J. H.; Moser, J. E.; Grätzel, M.; Park, N. G. Lead Iodide Perovskite Sensitized All-Solid-State Submicron Thin Film Mesoscopic Solar Cell with Efficiency Exceeding 9%. *Sci. Rep.* **2012**, *2*, No. 591.

(4) Kojima, A.; Teshima, K.; Shirai, Y.; Miyasaka, T. Organometal Halide Perovskites as Visible-Light Sensitizers for Photovoltaic Cells. *J. Am. Chem. Soc.* **2009**, *131*, 6050−6051.

(5) Zhou, H.; Chen, Q.; Li, G.; Luo, S.; Song, T.-B.; Duan, H.-S.; Hon, Z.; You, J.; Liu, Y.; Yang, Y. Interface Engineering of Highly Efficient Perovskite Solar Cells. *Science* **2014**, *345*, 542−546.

(6) NREL Best Research-Cell Efficiencies, March 2021, https://www.nrel.gov/pv/cell-efficiency.html.

(7) Stranks, S. D.; Eperon, G. E.; Grancini, G.; Menelaou, C.; Alcocer, M. J. P.; Leijtens, T.; Herz, L. M.; Petrozza, A.; Snaith, H. J. Electron-Hole Diffusion Lengths Exceeding 1 Micrometer in an Organometal Trihalide Perovskite Absorber. *Science* **2013**, *342*, 341−344.

(8) Hutter, E. M.; Eperon, G. E.; Stranks, S. D.; Savenije, T. J. Charge Carriers in Planar and Meso-Structured Organic-Inorganic Perovskites: Mobilities, Lifetimes, and Concentrations of Trap States. *J. Phys. Chem. Lett.* **2015**, *6*, 3082−3090.

(9) Cao, Y.; Wang, N.; Tian, H.; Guo, J.; Wei, Y.; Chen, H.; Miao, Y.; Zou, W.; Pan, K.; He, Y.; Cao, H.; Ke, Y.; Xu, M.; Wang, Y.; Yang, M.; Du, K.; Fu, Z.; Kong, D.; Dai, D.; Jin, Y.; Li, G.; Li, H.; Peng, Q.; Wang, J.; Huang, W. Perovskite Light-Emitting Diodes Based on Spontaneously Formed Submicrometre-Scale Structures. *Nature* **2018**, *562*, 249−253.

(10) Saliba, M.; Wood, S. M.; Patel, J. B.; Nayak, P. K.; Huang, J.; Alexander-Webber, J. A.; Wenger, B.; Stranks, S. D.; Horantner, M. T.; Wang, J. T.; Nicholas, R. J.; Herz, L. M.; Johnston, M. B.; Morris, S. M.; Snaith, H. J.; Riede, M. K. Structured Organic-Inorganic Perovskite toward a Distributed Feedback Laser. *Adv. Mater.* **2016**, *28*, 923−929.

(11) Wei, H.-S.; Fang, Y.; Mulligan, P.; Chuirazzi, W.; Fang, H.-H.; Wang, C.; Ecker, B. R.; Gao, Y.; Loi, M. A.; Cao, L.; Huang, J. Sensitive X-Ray Detectors Made of Methylammonium Lead Tribromide Perovskite Single crystals. *Nat. Photonics* **2016**, *10*, 333−340.

(12) Mcmeekin, D. P.; Sadoughi, G.; Rehman, W.; Eperon, G. E.; Saliba, M.; HöRantner, M. T.; Haghighirad, A.; Sakai, N.; Korte, L.; Rech, B.; Johnston, M. B.; Herz, L. M.; Snaith, H. J. A Mixed-Cation Lead Mixed-Halide Perovskite Absorber for Tandem Solar Cells. *Science* **2016**, *351*, 151−154.

(13) Park, I. J.; Park, J. H.; Ji, S. G.; Park, M.-A.; Jang, J. H.; Kim, J. Y. A Three-Terminal Monolithic Perovskite/Si Tandem Solar Cell Characterization Platform. *Joule* **2019**, *3*, 807−818.

(14) Futscher, M. H.; Ehrler, B. Efficiency Limit of Perovskite/Si Tandem Solar Cells. *ACS Energy Lett.* **2016**, *1*, 863−868.

(15) Albrecht, S.; Saliba, M.; Correa Baena, J. P.; Lang, F.; Kegelmann, L.; Mews, M.; Steier, L.; Abate, A.; Rappich, J.; Korte, L.; Schlatmann, R.; Nazeeruddin, M. K.; Hagfeldt, A.; Grätzel, M.; Rech, B. Monolithic Perovskite/Silicon-Heterojunction Tandem Solar Cells Processed at Low Temperature. *Energy Environ. Sci.* **2016**, *9*, 81−88.

(16) Heo, J. H.; Im, S. H. $CH_3NH_3PbBr_3$-$CH_3NH_3PbI_3$ Perovskite-Perovskite Tandem Solar Cells with Exceeding 2.2 V Open Circuit Voltage. *Adv. Mater.* **2016**, *28*, 5121−5125.

(17) Ulatowski, A. M.; Wright, A. D.; Wenger, B.; Buizza, L. R. V.; Motti, S. G.; Eggimann, H. J.; Savill, K. J.; Borchert, J.; Snaith, H. J.; Johnston, M. B.; Herz, L. M. Charge-Carrier Trapping Dynamics in Bismuth-Doped Thin Films of $MAPbBr_3$ Perovskite. *J. Phys. Chem. Lett.* **2020**, *11*, 3681−3688.

(18) Droseros, N.; Longo, G.; Brauer, J. C.; Sessolo, M.; Bolink, H. J.; Banerji, N. Origin of the Enhanced Photoluminescence Quantum Yield in $MAPbBr_3$ Perovskite with Reduced Crystal Size. *ACS Energy Lett.* **2018**, *3*, 1458−1466.

(19) Baranowski, M.; Plochocka, P. Excitons in Metal-Halide Perovskites. *Adv. Energy Mater.* **2020**, *10*, No. 1903659.

(20) Aydin, E.; De Bastiani, M.; De Wolf, S. Defect and Contact Passivation for Perovskite Solar Cells. *Adv. Mater.* **2019**, *31*, No. 1900428.

(21) Wu, C. G.; Chiang, C. H.; Chang, S. H. A Perovskite Cell with A Record-High-V_{oc} of 1.61 V Based on Solvent Annealed $CH_3NH_3PbBr_3$/ICBA Active Layer. *Nanoscale* **2016**, *8*, 4077−4085.

(22) Liu, Z.; Krückemeier, L.; Krogmeier, B.; Klingebiel, B.; Márquez, J. A.; Levcenko, S.; Öz, S.; Mathur, S.; Rau, U.; Unold, T.; Kirchartz, T. Open-Circuit Voltages Exceeding 1.26 V in Planar Methylammonium Lead Iodide Perovskite Solar Cells. *ACS Energy Lett.* **2019**, *4*, 110−117.

(23) Jiang, X.; Hoffman, J.; Stoumpos, C. C.; Kanatzidis, M. G.; Harel, E. Transient Sub-Band-Gap States at Grain Boundaries of $CH_3NH_3PbI_3$ Perovskite Act as Fast Temperature Relaxation Centers. *ACS Energy Lett.* **2019**, *4*, 1741−1747.

(24) Chen, B.; Rudd, P. N.; Yang, S.; Yuan, Y.; Huang, J. Imperfections and Their Passivation in Halide Perovskite Solar Cells. *Chem. Soc. Rev.* **2019**, *48*, 3842−3867.

(25) Motti, S. G.; Meggiolaro, D.; Martani, S.; Sorrentino, R.; Barker, A. J.; De Angelis, F.; Petrozza, A. Defect Activity in Lead Halide Perovskites. *Adv. Mater.* **2019**, *31*, No. 1901183.

(26) Musiienko, A.; Pipek, J. I.; Praus, P.; Brynza, M.; Belas, E.; Dryzhakov, B.; Du, M.-H.; Ahmadi, M.; Grill, R. Deciphering the Effect of Traps on Electronic Charge Transport Properties of Methylammonium Lead Tribromide Perovskite. *Sci. Adv.* **2020**, *6*, No. eabb6393.

(27) Zhang, W.; Pathak, S.; Sakai, N.; Stergiopoulos, T.; Nayak, P. K.; Noel, N. K.; Haghighirad, A. A.; Burlakov, V. M.; Dequilettes, D. W.; Sadhanala, A.; Li, W.; Wang, L.; Ginger, D. S.; Friend, R. H.; Snaith, H. J. Enhanced Optoelectronic Quality of Perovskite Thin Films with Hypophosphorous Acid for Planar Heterojunction Solar Cells. *Nat. Commun.* **2015**, *6*, No. 10030.

(28) Abzieher, T.; Mathies, F.; Hetterich, M.; Welle, A.; Lemmer, U.; Paetzold, U. W.; Powalla, M.; et al. Additive-Assisted Crystallization Dynamics in Two-Step Fabrication of Perovskite Solar Cells. *Phys. Status Solidi (A)* **2017**, *214*, No. 1700509.

(29) Leijtens, T.; Eperon, G. E.; Barker, A. J.; Grancini, G.; Zhang, W.; Ball, J. M.; Kandada, A. R. S.; Snaith, H. J.; Petrozza, A. Carrier Trapping and Recombination: the Role of Defect Physics in Enhancing the Open Circuit Voltage of Metal Halide Perovskite Solar Cells. *Energy Environ. Sci.* **2016**, *9*, 3472−3481.

(30) Shi, D.; Adinolfi, V.; Comin, R.; Yuan, M.; Alarousu, E.; Buin, A.; Chen, Y.; Hoogland, S.; Rothenberger, A.; Katsiev, K.; Losovyj, Y.; Zhang, X.; Dowben, P. A.; Mohammed, O. F.; Sargent, E. H.; Bakr, O. M. Low Trap-State Density and Long Carrier Diffusion in Organolead Trihalide Perovskite Single Crystals. *Science* **2015**, *347*, 519−522.

(31) Caselli, V. M.; Wei, Z.; Ackermans, M. M.; Hutter, E. M.; Ehrler, B.; Savenije, T. J. Charge Carrier Dynamics upon Sub-bandgap Excitation in Methylammonium Lead Iodide Thin Films: Effects of Urbach Tail, Deep Defects, and Two-Photon Absorption. *ACS Energy Lett.* **2020**, *5*, 3821−3827.

(32) Hutter, E. M.; Hofman, J. J.; Petrus, M. L.; Moes, M.; Abello'N, R. D.; Docampo, P.; Savenije, T. J. Charge Transfer from Methylammonium Lead Iodide Perovskite to Organic Transport Materials: Efficiencies, Transfer Rates, and Interfacial Recombination. *Adv. Energy Mater.* **2017**, *7*, No. 1602349.

(33) Savenije, T. J.; Guo, D.; Caselli, V. M.; Hutter, E. M. Quantifying Charge-Carrier Mobilities and Recombination Rates in Metal Halide Perovskites from Time-Resolved Microwave Photoconductivity Measurements. *Adv. Energy Mater.* **2020**, No. 1903788.

(34) Herz, L. M. Charge-Carrier Mobilities in Metal Halide Perovskites: Fundamental Mechanisms and Limits. *ACS Energy Lett.* **2017**, *2*, 1539−1548.

(35) Guo, D.; Andaji Garmaroudi, Z.; Abdi-Jalebi, M.; Stranks, S. D.; Savenije, T. J. Reversible Removal of Intermixed Shallow States by Light Soaking in Multication Mixed Halide Perovskite Films. *ACS Energy Lett.* **2019**, *4*, 2360−2367.

(36) Abdi-Jalebi, M.; Andaji-Garmaroudi, Z.; Cacovich, S.; Stavrakas, C.; Philippe, B.; Richter, J. M.; Alsari, M.; Booker, E. P.; Hutter, E. M.; Pearson, A. J.; Lilliu, S.; Savenije, T. J.; Rensmo, H.; Divitini, G.; Ducati, C.; Friend, R. H.; Stranks, S. D. Maximizing and Stabilizing Luminescence from Halide Perovskites with Potassium Passivation. *Nature* **2018**, *555*, 497−515.

(37) Noel, N. K.; Congiu, M.; Ramadan, A. J.; Fearn, S.; Mcmeekin, D. P.; Patel, J. B.; Johnston, M. B.; Wenger, B.; Snaith, H. J. Unveiling the Influence of pH on the Crystallization of Hybrid Perovskites, Delivering Low Voltage Loss Photovoltaics. *Joule* **2017**, *1*, 328−343.

(38) Luo, D.; Su, R.; Zhang, W.; Gong, Q.; Zhu, R. Minimizing Non-Radiative Recombination Losses in Perovskite Solar Cells. *Nat. Rev. Mater.* **2020**, *5*, 44−60.

(39) Sestu, N.; Cadelano, M.; Sarritzu, V.; Chen, F.; Marongiu, D.; Piras, R.; Mainas, M.; Quochi, F.; Saba, M.; Mura, A.; Bongiovanni, G. Absorption F-Sum Rule for the Rxciton Binding Energy in Methylammonium Lead Halide Perovskites. *J. Phys. Chem. Lett.* **2015**, *6*, 4566−4572.

(40) Reid, O. G.; Yang, M.; Kopidakis, N.; Zhu, K.; Rumbles, G. Grain-Size-Limited Mobility in Methylammonium Lead Iodide Perovskite Thin Films. *ACS Energy Lett.* **2016**, *1*, 561−565.

(41) Shi, D.; Qin, X.; Li, Y.; He, Y.; Zhong, C.; Pan, J.; Dong, H.; Xu, W.; Li, T.; Hu, W.; Bre′Das, J. L.; Bakr, O. M. Spiro-OMeTAD Single Crystals: Remarkably Enhanced Charge-Carrier Transport via Mesoscale Ordering. *Sci. Adv.* **2016**, *2*, No. e1501491.

(42) Liang, P.-W.; Chueh, C.-C.; Williams, S. T.; Jen, A. K. Y. Roles of Fullerene-Based Interlayers in Enhancing the Performance of Organometal Perovskite Thin-Film Solar Cells. *Adv. Energy Mater.* **2015**, *5*, No. 1402321.